

Unified description over time of heterogeneous condensation with quenched disorder

Supplementary material

Ruddy Urbina* and Wenceslao González-Viñas†

Universidad de Navarra, Dept. of Physics and Applied Mathematics, Pamplona, Spain

(Dated: December 8, 2023)

I. EXPERIMENTAL DETAILS

At the given conditions, the streamed humid air (70% RH, 21 °C) to a substrate at 10 °C, corresponds to a supersaturation (p_w/p_s , being p_w the actual partial pressure of water vapor, and p_s the water saturation pressure (a.k.a. vapor pressure) at 10 °C) of 1.416. Assuming that the necessary supersaturation for initiating homogeneous condensation is 2.4 [1], we can conclude that under the conditions of our experiment, a contact angle equal to or less than 60° is required to initiate condensation with a supersaturation of 1.416. The contact angles are in all the experiments bigger than this value (table I) and consequently condensation only takes place in impurities/imperfections where effective (local) contact angle is much smaller than the measured macroscopic one. This favors the existence of quenched disorder.

TABLE I. Immersion time (in minutes) in the coating process with concentration c (in % (v/v)), advancing θ_a , receding θ_r and average θ_m contact angles of each sample, with their corresponding volume coefficient γ , and contact angle hysteresis H . The labels of the coated substrates have been assigned based on the actual nucleation densities.

Label	Time	c	θ_a (°)	θ_r (°)	θ_m (°)	γ_a	γ_r	H
None	N/A	N/A	91	62	76.5	2.15	1.06	0.19
Low	10	0.8	130	79	104.5	3.84	1.59	0.24
Intermediate	10	0.5	120	93	106.5	3.53	2.26	0.13
High	5	1.0	124	96	110	3.67	2.42	0.13

The value of the contact angle hysteresis H in Table I is calculated as $H = \frac{\theta_a - \theta_r}{\theta_a + \theta_r}$ [2]. There are other measurements of hysteresis (e.g. $\cos \theta_r - \cos \theta_a$ [3]), but they give qualitatively an equivalent information.

Being the supersaturation 1.416, we can calculate the critical radius (of curvature) of a stable nucleated cluster by using Eq. 9-15 of [4], valid for heterogeneous nucleation. In our conditions, it turns out to be 3.1 nm. That corresponds to an initial apparent radius (depending on the experiment contact angles) between 2.7 nm to 3.1 nm. With our experimental set-up, we are not able to detect these tiny droplets.

II. NUCLEATION

The coating of the substrates with OTS + HMDSO leaves them with many imperfections/impurities coming from the resulting precipitate. These imperfections may or may not be nucleation sites, which are points where the energy barrier to nucleate is much smaller than in the surroundings. Additionally, there may be nucleation sites on the substrate that cannot be resolved with our experimental setup. However, under our experimental conditions, these sites remain at static positions and do not relax within the timescales of our experiments.

In Fig. 1, we present snapshots from the experiments taken at very short times (prior to the experimental conditions becoming stationary). The snapshot captured at 0 s was taken before the experiment began, where imperfections/impurities are clearly visible. At 6 s, numerous spots can be observed which correspond to nucleation sites (on imperfections/impurities, whether visible or not at 0 s). At 12 s and 60 s, some droplets have grown sufficiently to be distinguished on the substrate. The figure illustrates some imperfections/impurities [at 0 s] that evolve into standard growing droplets (e.g. **a**), some imperfections that seem not to be nucleation sites (e.g. **b**) and retain their shape and size throughout the experiment, and others (e.g. **c**) that transform into condensed droplets [in the example, at 12 s] that later evaporate. Additionally, there are locations in the figure that are undetectable at 0 s, but appear as spots at 6 s. Some of them develop into standard growing droplets (e.g. **d**), some remain the same shape and size once they appear at 6 s (e.g. **e**), and others (e.g. **f**) transform into droplets [in the example, at 12 s] that subsequently evaporate.

Loci (spots/imperfections/impurities) that do not evolve into clearly detectable droplets after 180 seconds are called passive sites and are not considered in this work. We have named the remaining sites active sites.

The evaporation of droplets (e.g., **c** and **f**) is often observed at times smaller than 180 s, that we do not consider in this work. It is possible that this evaporation occurs in a concentration gradient caused by a nearby larger droplet.

III. COALESCENCE EVENTS IN DROPLETS

At the starting time of the studied period, we see few coalescence events amongst the growth by diffusion of wa-

* rurbina@alumni.unav.es

† Corresponding author: wens@unav.es

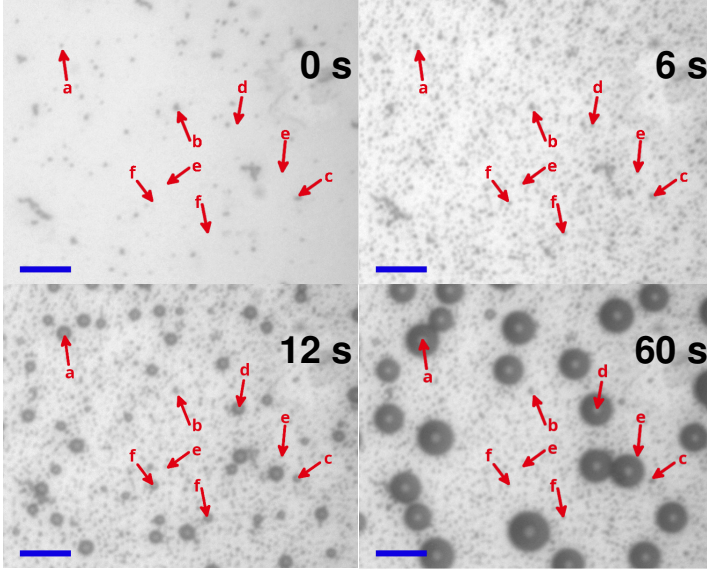


FIG. 1. Early moments of the Intermediate experiment are shown before it can be ensured that the experimental conditions have reached the stationary state. The scale bars correspond to $10 \mu\text{m}$, and arrows indicate examples of different features (see text).

ter molecules. Very rarely we can observe droplets that disappear or reduce their size. All the change in the number of droplets comes from coalescence events. In Fig. 2 we can see two representative examples (in Low and None cases) of consecutive snapshots at the beginning of the studied period. Coalescence events are marked by red squares enclosing the coalesced droplet (see right images of the figure, b and d). Coalescence events are few and do not dominate the evolution of the BF.

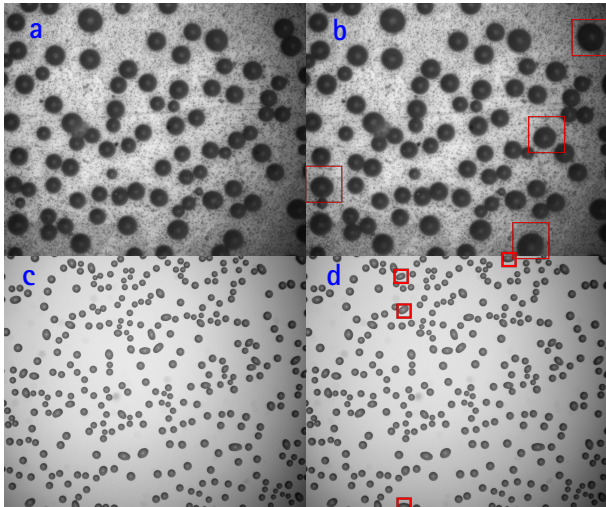


FIG. 2. BF at the beginning of the reported data. (a) Low case, 180 s (b) Low case, 210 s (c) None case, 180 s and (d) None case, 190 s. HFOV: (a, b) 0.220 mm and (c, d) 1.104 mm. Red squares are hints to coalescence events.

In our experiments, droplets coalesce either with momentum conservation due to low dissipation (coated substrates) or with very high dissipation at the three-phase contact line (bare substrates) [1, 5]. In the former case, droplets recover their spherical cap shape promptly (in less than 6 seconds, which is the time between frames in that part of the experiment), as shown in Fig. 3. In the latter case, the contact line is pinned, and the droplets only recover their shape at longer times due to the growth of the droplet by water molecule diffusion into the droplet. This is illustrated in Fig. 4, where the shape is almost recovered after around 15 minutes.

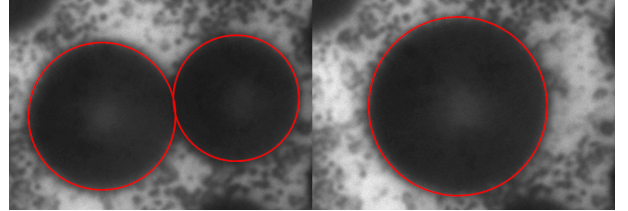


FIG. 3. Representative coalescence event for the coated substrates (High, Intermediate, and Low). In the figure, a region of interest before (left) and after (right) the event, for the High experiment. The scale is the same for both images, and is given by the diameter of the rightmost droplet (coalesced), which is $30.8 \mu\text{m}$. The left image corresponds to a time of 666 s and the right image to a time of 672 s.

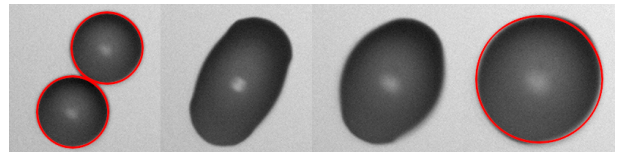


FIG. 4. Representative coalescence event for the bare substrates (None). In the figure, a region of interest before (left-most) and after (right) the event, for the None experiment. The scale is the same for the four images, and is given by the diameter of the rightmost droplet (coalesced, and almost hemispherical), which is $79.6 \mu\text{m}$. The leftmost image corresponds to a time of 580 s and the following (from left to right) to: 582 s, 883 s, and 1453 s.

The result of a coalescence event can be characterized by the center of mass of the coalesced droplet with respect to the coalescing droplets [1, 5]. Given two coalescing droplets i and j resulting in the droplet k , the relative radius asymmetry can be defined as $\nu \equiv \frac{R_i}{R_i + R_j}$. Here, we will assume, without any restriction, that droplet i is larger than droplet j . In this case, $\nu \in [0.5, 1)$, and affects the position (of the center of mass) of the resulting droplet. By taking the position of the larger droplet (i) as the origin of coordinates, we can define the displacement of the coalesced droplet as follows: $\vec{r}_k - \vec{r}_i \equiv \Psi(\nu) [\vec{r}_j - \vec{r}_i]$. For negligible or strong contact line pinning, it can be proven that $\Psi(\nu) = \frac{(1-\nu)^3}{\nu^3 + (1-\nu)^3}$.

In an experiment, intrinsic measurement errors may

cause $\Psi(\nu)$ to be ill-defined due to the existence of a perpendicular component, which could also arise from heterogeneity in the contact line pinning. We consider the perpendicular component as an estimate of the error. Figs. 5 and 6 show plots of $\Psi(\nu)$ for the None and Intermediate cases, respectively.

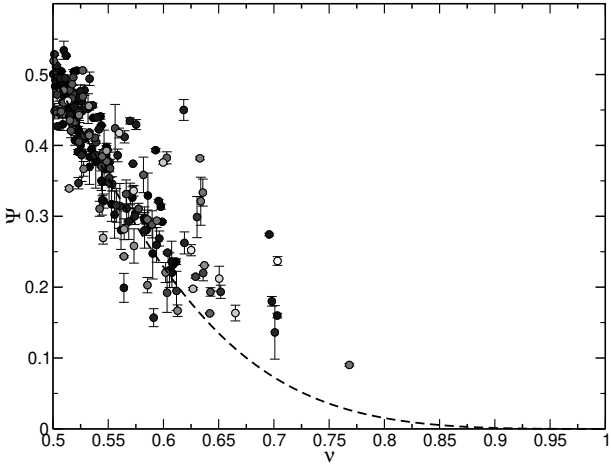


FIG. 5. Dimensionless center of mass Ψ as a function of the relative radius asymmetry ν for the case None. The dashed line represents the prediction for negligible or strong contact line pinning. The grayscale saturation values of the data points refer to different times, where black corresponds to 180 s and white to 3643 s. The error bars correspond to the perpendicular component appearing in the definition of Ψ (see text) and are included for reference purposes only.

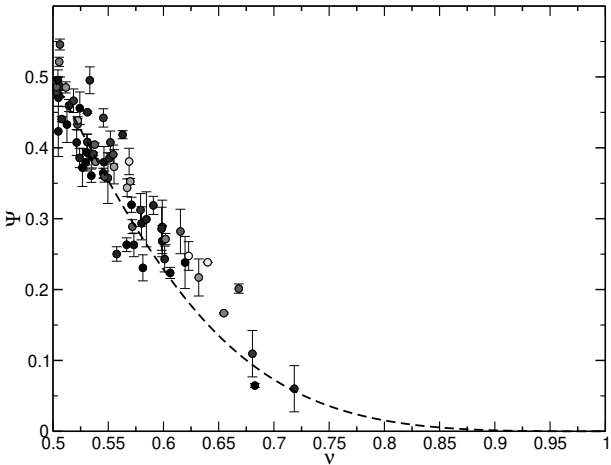


FIG. 6. Dimensionless center of mass Ψ as a function of the relative radius asymmetry ν for the case Intermediate. The dashed line represents the prediction for negligible or strong contact line pinning. The grayscale saturation values of the data points refer to different times, where black corresponds to 180 s and white to 1020 s. The error bars correspond to the perpendicular component appearing in the definition of Ψ (see text) and are included for reference purposes only.

IV. TIME SCALES

In our system, nucleation occurs almost instantly at the start of the experiment, and the dynamics of Breath Figures are a result of the interplay between diffusion-driven growth and coalescence. Coalescence events occur on significantly short time scales, estimated to be smaller than tens of milliseconds in our specific experimental conditions (see table 5.1 of [1]). These timescales are notably shorter compared to our measured characteristic time, which is on the order of hundreds of seconds, allowing us to disregard them. As a result, the influence of coalescence on the dynamics is purely from statistical and geometrical aspects of the system, primarily the spatial distribution of drops.

Therefore, diffusion stands as the primary microscopic mechanism governing Breath Figure evolution. However, it's important to note that diffusion-driven growth is also influenced by boundary conditions and the surface number density of droplets. Across all our experiments, the local parameters are the same and remain constant. Consequently, a characteristic time associated with diffusion is determined, and varies only due to changes in the surface number density. This time arises from the individual growth law $r_i(t) = (r_{i_0} + Dt)^{\frac{1}{\alpha}} \equiv r_{i_0}(1 + t/\tau_{\text{diff}})^{\frac{1}{\alpha}}$, giving $\tau_{\text{diff.}} = r_{i_0}^{\alpha}/D = \gamma\rho_0 r_{i_0}^{\alpha}/C$. Here, C is the same throughout all experiments. Additionally, $\tau_{\text{diff.}}$ is markedly smaller, on the order of microseconds or less (based on the calculated value of D [1]), when compared to the measured characteristic time.

The only relevant remaining time is dictated by the structure of the Breath Figure and the collective coalescence behavior, that primarily influences the evolution of the surface number density. Equations 2 and 3 in the main text outline this time (τ), which is the sole pertinent time frame in our investigation. It's important to highlight that this derived time is also dependent on the growth of the droplets themselves, as described by equation 2 in the main text.

In summary, the characteristic times (τ) defined by equations 2 and 3 in the main text vary only between experiments due to the statistical and geometrical aspects of the system. As previously mentioned, the other parameters influencing individual growth time scales are the same across all our experiments. In a CSR, the statistical and geometrical aspects are primarily contingent upon the initial number density of the droplets. Higher number densities result in earlier droplet coalescence due to their proximity. Conversely, higher number densities delay the diffusion-driven growth of the droplets because the available humidity must be distributed among more droplets.

As the parameter α increases (in our case, $\alpha = 3$), the importance of diffusion-driven growth diminishes, and the competition leans towards coalescence. As a result, the characteristic time aligns with the physics of coalescence. In this scenario ($\alpha > 2$), when the initial number density (ρ_0) increases, τ decreases, leading to faster dy-

namics in number density. However, the trade-off is that individual droplets grow more slowly through diffusion (see Fig. 7, and Table II).

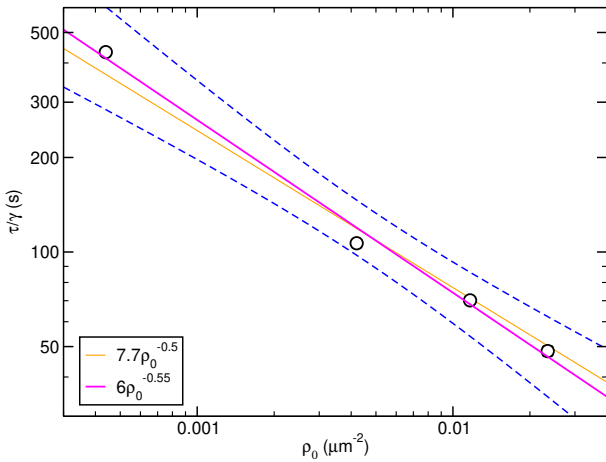


FIG. 7. Relationship between the characteristic time τ/γ and the initial number density ρ_0 for the different studied cases. Dark (magenta) solid line is the best fit to a power law, and the light (orange) solid line is the fit to a power law with the expected exponent (-0.5). Dashed lines represent the boundaries of the confidence band to the power line fit.

TABLE II. Obtained values for τ and ρ_0 for each sample. The errors correspond to a 95% confidence interval.

Label	τ (10^2 s)	ε_τ (10^2 s)	ρ_0 (μm^{-2})	ε_{ρ_0} (μm^{-2})
None	9.30	0.06	4.39×10^{-4}	2×10^{-6}
Low	4.09	0.13	4.2×10^{-3}	10^{-4}
Intermediate	2.48	0.07	1.17×10^{-2}	4×10^{-4}
High	1.77	0.07	2.3×10^{-2}	10^{-3}

V. SIZE DISTRIBUTION

The size distribution of droplets has been widely considered in the literature (see, among others: [5–11]). Before considering the size distribution of droplets in our system, some complementary considerations must be taken into account.

One of our assumptions when fitting magnitudes related to moments of the size distribution is that $\langle r^j \rangle / \langle r \rangle^j$ remains approximately constant over time for any $j \in \mathbb{Z}$ up to order k (i.e., $0 \leq j \leq k$). Under very general conditions, it can be proven that the probability density function $f(r, t)$ must have the following form to fulfill this condition:

$$f(r, t) = \frac{a}{\langle r \rangle} h\left(b \frac{r}{\langle r \rangle}\right), \quad (1)$$

where h is any (non-negative) real function with finite moments μ_j up to order k . Here:

$$\mu_j \equiv \int_0^\infty x^j h(x) dx < +\infty, \quad (2)$$

In Eq. 1, $a = \frac{\mu_1}{\mu_0^2}$ and $b = \frac{\mu_1}{\mu_0}$.

All temporal dependence in f is through $\langle r \rangle$ itself. We would like to point out that in this case, data dispersion can occur (e.g., $\sigma^2 \neq 0$). In fact, $\sigma^2 = \langle r \rangle^2 \left(\frac{\mu_0 \mu_2}{\mu_1^2} - 1 \right)$.

In Fig. 8, we have plotted the coefficient of variation ($\sigma_r / \langle r \rangle$). It can be observed that this value is approximately constant in all cases, except for the High density case at long times ($t > 9\tau$).

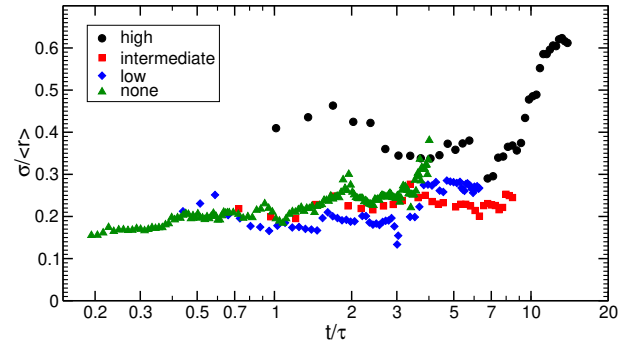


FIG. 8. Coefficient of variation ($\sigma_r / \langle r \rangle$) vs dimensionless time.

In Fig. 9, we present the scaled probability density function at three different times. This behavior is representative of the Intermediate, Low, and None cases. The three curves almost collapse, taking into account the statistical error.

However, small variations impede a collapse of the h function at different times in the High density case (see Fig. 10).

In Fig. 11, we plot the dimensionless number density of droplets as a function of the dimensionless radii at a dimensionless time of 1.01 ± 0.02 . We observe that the High case is quite different from the others and has a component of the distribution of small droplets that is absent in the other cases. Despite this difference, the same macroscopic scaling allows for a collapse of the relevant data, as shown in the main text of the Article.

In Figs. 12 and 13 we can see the distribution of sizes (proportional to the volume of droplets), scaled in different ways to compare with Fig. 3b of [11] and Fig. 1b of [10], respectively.

Note that in Fig. 13 we scaled the size of the droplets (x-axis) with their maximum value, unlike what they do when taking an average value of the bump. Due to the

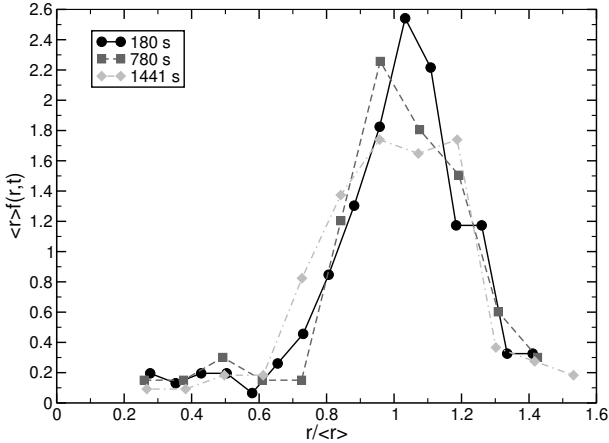


FIG. 9. Scaled probability density function versus radius, scaled with its average radius, for the Intermediate density case at three different times.

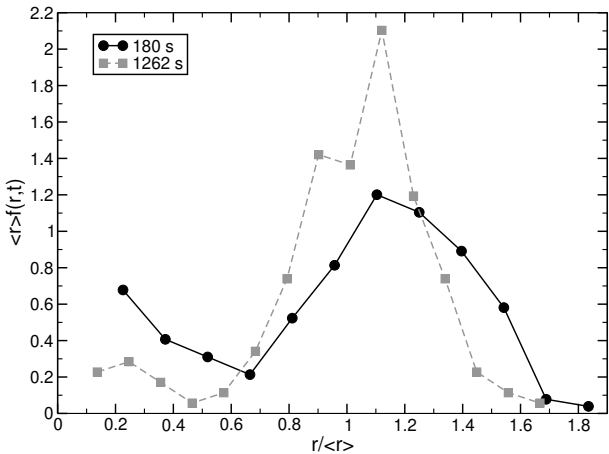


FIG. 10. Scaled probability density function versus radius, scaled with its average radius, for the High density case at two different times.

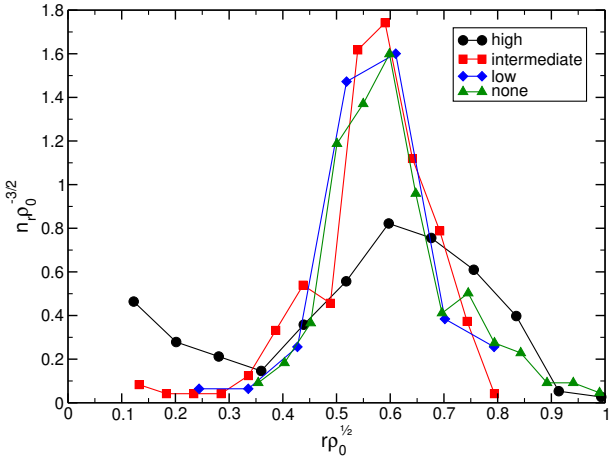


FIG. 11. Dimensionless number density of droplets as a function of the dimensionless radii, for the considered experiments at dimensionless time 1.01.

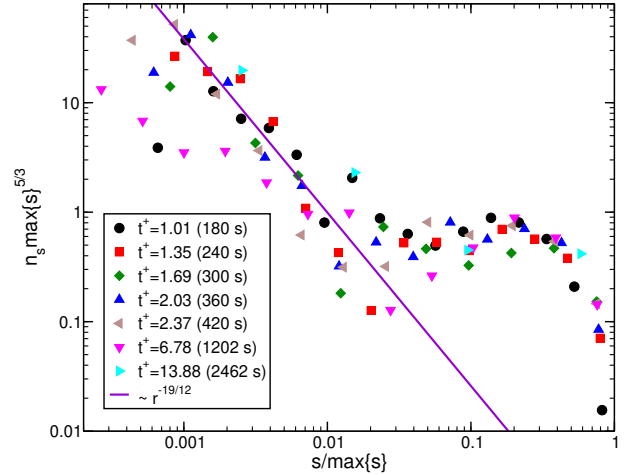


FIG. 12. r^3 distribution of the droplets at several times. The labels of each curve give the dimensionless time and in parenthesis the physical time. The solid line is a guide for the eye representing the theoretical prediction given in [11]

ambiguity in the definition of said average value (more relevant in our case), we prefer to take the maximum global value instead.

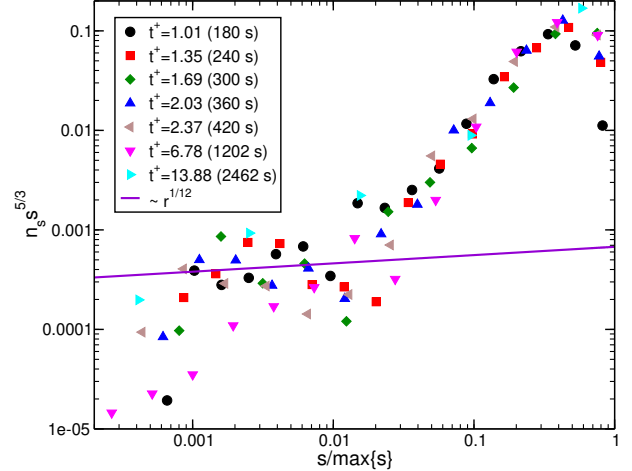


FIG. 13. r^3 distribution of the droplets at several times. The labels of each curve give the dimensionless time and in parenthesis the physical time. The solid line is a guide for the eye representing the theoretical prediction given in [10]

In Fig. 14, we plot data from the r^3 distributions of droplets for the different coated substrates. $s \equiv r^3$ is made dimensionless with the maximum value for each substrate. To distinguish between regimes (power law vs universal scaling) observed in [10, 11] we separate the data in times smaller, and bigger, than the average relaxation time of the density $\rho/\rho_0 = \exp(-t^{+2/3})$, calculated as the area under the curve. It is straightforward to obtain that the average relaxation (dimensionless) time is $\frac{3}{4}\sqrt{\pi} \approx 1.33$. We consider this time to be the criti-

cal value from which coalescence starts to dominate, although other measures (e.g. when average radius starts to grow as time, when the surface coverage reaches the plateau, ...) will give longer times. Full solid symbols correspond to dimensionless times smaller than 1.33. The lists of plotted distributions times are the following. For the High case, the same as in Fig. 13 (see corresponding legend), while for the Intermediate case: 0.73, 0.97, 1.21, 1.45, 1.68 and 5.08; for the Low case: 0.44, 0.59, 0.73, 0.88, 1.03 and 2.93; and for the None case: 0.19, 0.26, 0.32, 0.39, 0.45, 1.30, 3.14.

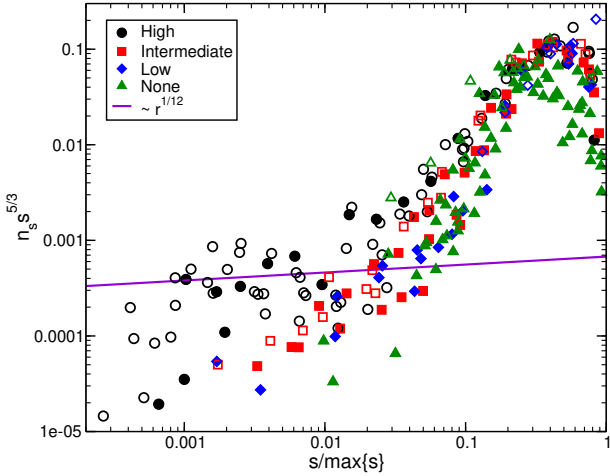


FIG. 14. r^3 distribution of the droplets for the different coating conditions. Solid (open) symbols correspond to dimensionless times smaller (bigger) than 1.33 (see text). The solid line is a guide for the eye representing the theoretical prediction given in [10]

Some of the snapshots of our experiments don't have

enough droplets to get good statistical significance for the droplet size distribution, preventing us from empirically obtaining the general form of the distributions. However, the distributions shed light on some issues: the bump (right side of the distribution) is not symmetric (in log scale) relative to its maximum, and there is not a dip that separates the bump from the tails (left side of the distribution). Indeed, the tails can only be observed clearly in some times of the High case. The reason is double: on the one hand, there are no new nucleation events on empty regions of the substrate without imperfections (due to the static nucleation sites characteristic of the quenched disorder and to the experiments supersaturation below the critical one) that otherwise would continuously feed the distribution lower end (left side). On the other hand, coalescence events deplete the left side at short times. All of this sets our results clearly apart from what is found in previous literature.

ACKNOWLEDGMENTS

This work was partly supported by the Spanish MCIN/AEI/10.13039/501100011033 (Grants FIS2017-83401-P and PID2021-129066NA-I00) and by “ERDF A way of making Europe”. R.U. acknowledges financial support from the “Asociación de Amigos de la Universidad de Navarra”. We thank Luis Fernando Urrea for technical support, and the anonymous reviewers for fruitful suggestions.

R.U. conducted the experiments, and W.G. analyzed the results presented in this Supplementary material and wrote its first draft version. Both authors contributed equally to the other tasks.

-
- [1] D. Beysens, *The Physics of Dew, Breath Figures and Dropwise Condensation* (Springer, 2022).
 - [2] H. Zhao and D. Beysens, From Droplet Growth to Film Growth on a Heterogeneous Surface: Condensation Associated with a Wettability Gradient, *Langmuir* **11**, 627 (1995).
 - [3] J. Trosseille, A. Mongruel, L. Royon, M.-G. Medici, and D. Beysens, Roughness-enhanced collection of condensed droplets, *The European Physical Journal E* **42**, 144 (2019).
 - [4] H. R. Pruppacher and J. D. Klett, *Microphysics of Clouds and Precipitation*, second revised and enlarged ed., ATMOSPHERIC AND OCEANOGRAPHIC SCIENCES LIBRARY, Vol. 18 (Kluwer Academic Publishers, 2004).
 - [5] J. L. Viovy, D. Beysens, and C. M. Knobler, Scaling description for the growth of condensation patterns on surfaces, *Phys. Rev. A* **37**, 4965 (1988).
 - [6] F. Family and P. Meakin, Kinetics of droplet growth processes: Simulations, theory and experiments, *Phys. Rev. A* **40**, 3836 (1989).
 - [7] D. Beysens, C. M. Knobler, and H. Schaffar, Scaling in the growth of aggregates on a surface, *Phys. Rev. B* **41**, 9814 (1990).
 - [8] J. A. Blackman and S. Brochard, Polydispersity exponent in homogeneous droplet growth, *Phys. Rev. Lett.* **84**, 4409 (2000).
 - [9] R. N. Leach, F. Stevens, S. C. Langford, and J. T. Dickinson, Dropwise condensation: Experiments and simulations of nucleation and growth of water drops in a cooling system, *Langmuir* **22**, 8864 (2006).
 - [10] J. Blaschke, T. Lapp, B. Hof, and J. Vollmer, Breath figures: Nucleation, growth, coalescence, and the size distribution of droplets, *Phys. Rev. Lett.* **109**, 068701 (2012).
 - [11] L. Stricker, F. Grillo, E. A. Marquez, G. Panzarasa, K. Smith-Mannschott, and J. Vollmer, Universality of breath figures on two-dimensional surfaces: An experimental study, *Phys. Rev. Research* **4**, L012019 (2022).